Dissipation Range Dynamics: Kinetic Alfvén Waves and the Importance of β_e

Robert J. Leamon, Charles W. Smith, Norman F. Ness,[1]
and
Hung K. Wong[2]

[1] *all at Bartol Research Institute, University of Delaware, Newark, DE*
[2] *Aurora Science Inc., San Antonio, TX*

Abstract. In a previous paper we argued that the damping of obliquely propagating kinetic Alfvén waves, chiefly by resonant mechanisms, was a likely explanation for the formation of the dissipation range for interplanetary magnetic field fluctuations. This suggestion was based largely on observations of the dissipation range at 1 AU as recorded by the Wind spacecraft. We pursue this suggestion here with both a general examination of the damping of obliquely propagating kinetic Alfvén waves and an additional examination of the observations. We explore the damping rates of kinetic Alfvén waves under a wide range of interplanetary conditions using numerical solutions of the linearized Maxwell-Vlasov equations and demonstrate that these waves display the nearly isotropic dissipation properties inferred from the previous paper. Using these solutions, we present a simple model to predict the onset of the dissipation range and compare these predictions to the observations. In the process we demonstrate that electron Landau damping plays a significant role in the damping of interplanetary magnetic field fluctuations which leads to significant heating of the thermal electrons.

— Submitted to *J. Geophys. Res.*, September 10, 1998; revised March 17, 1999; accepted March 23, 1999. —

1 INTRODUCTION

While it is now widely accepted that the interplanetary medium behaves to some degree as a turbulent magnetofluid [*Coleman*, 1968], little has been learned about the ultimate fate of the turbulent energy. Whether or not significant spectral transfer of the magnetic and velocity fluctuation energy is present [*Matthaeus et al.*, 1998] and regardless of how much of the fluctuation energy is produced *in situ* within the interplanetary medium [*Zank et al.*, 1996], there is now ample evidence that kinetic processes are dissipating the energy at the smallest fluid scales [*Behannon*, 1975; *Denskat et al.*, 1983; *Smith et al.*, 1990; *Goldstein et al.*, 1994].

Leamon et al. [1998a] (hereafter Paper 1) recently examined an ensemble of 33 quasi-stationary, 1-hour samples of high-resolution Wind observations from 1 AU and attempted to characterize the dissipation range spectra contained within the intervals. We found that dissipation range onset is consistently associated with spacecraft-frame frequencies comparable to, but greater than, the proton cyclotron frequency. Dissipation range spectral indices varied from -2.34 to -4.23 and averaged -3.01.

Helios [*Denskat et al.*, 1983] and Mariner observations [*Smith et al.*, 1990] inside 1 AU suggest that the dissipation range may fall more steeply in this region while Voyager observations [*Smith et al.*, 1990] from beyond 1 AU suggest the dissipation range may be a more shallow function of frequency beyond the Earth's orbit. However, these are only preliminary results and many more data intervals must be examined before this can be said conclusively. In all cases reported so far, it appears that the association of the dissipation range with frequencies comparable to the cyclotron frequency holds.

An additional conclusion of Paper 1 was that the onset of the dissipation range could not be predicted using simple resonant theories for parallel-propagating Alfvén waves. *Schwartz et al.* [1981] also concluded that the dissipation of solar-generated (*i.e.*, parallel-propagating), noninteracting Alfvén waves is insufficient to overcome adiabatic cooling of the (perpendicular component) of the solar wind. Both papers strongly suggest that wave vectors at oblique angles to the mean field play an important

role in the formation of the dissipation range, although in the case of Schwartz *et al.*, these waves are induced by ion beam driven instabilities.

The object of this paper is to test if the existence and subsequent damping of kinetic Alfvén waves can match the required properties of these inferred oblique waves. In section 2 we describe our data set used and present an example power spectrum of interplanetary magnetic field (IMF) fluctuations at 1 AU. A graph showing the relationship between the Larmor radius and the wavenumber at which dissipation sets in seems to suggest that a more isotropic dissipation mechanism is needed in addition to cyclotron resonant damping. In section 3 we investigate numerically the dispersion, dissipation and polarization properties of kinetic Alfvén waves, the effects of cyclotron-resonant and Landau damping, and how the effects of the two damping mechanisms change with changing ambient plasma parameters. Section 4 tests how well the observed IMF power spectra can be explained by damping of kinetic Alfvén waves. We construct a three-dimensional (3-D) spectrum $E(\mathbf{k})$ that is consistent with the observations, although not unique. From this 3-D spectrum we also calculate the heating rate due to damping of kinetic Alfvén waves, and compare it to the additional required heating due to the nonadiabatic temperature profile of the solar wind. We also compare the dissipation heating rate to the observed inertial-range turbulent cascade rate. Finally, in section 5 we compare the observed spectral break frequency to a prediction based on the damping of kinetic Alfvén waves for the Wind data intervals previously studied by us, and in section 6 we summarize our findings and the limitations of the underlying assumptions.

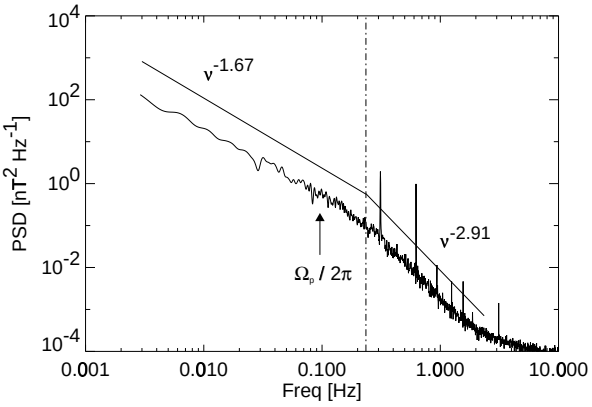

FIGURE 1. Trace of power spectral density matrix for hour 2200 UT, January 11, 1997, providing an example of dissipation range power spectrum at 1 AU. For this period, $B = 6.27$ nT, $\beta_p = 0.480$, $\Theta_{BV} = 38.1°$, $V_{SW} = 517$ km s^{-1}, and $\Omega_p = 0.605$ rad s^{-1} (0.096 Hz). The spectral break frequency is computed to be 0.235 Hz (marked by a vertical dashed line). Measurements were recorded by the WIND spacecraft.

2 OBSERVATIONS

In this paper we will again make use of the database of dissipation range spectra developed and analyzed in Paper 1. The 1-hour intervals of high-resolution magnetic field data from the Wind Magnetic Field Investigation (MFI) instrument [*Lepping et al.*, 1995] used in that study were chosen to be quasi-stationary and possessing well-defined power law energy spectra. A first-order difference filter was employed to remove linear trends from the data and a postdarkening filter corrected the resulting spectrum [*Chen*, 1989]. The previous analysis showed that the dissipation range is characterized by highly transverse magnetic fluctuations with transverse or oblique wavevectors that form a large fraction of the total energy. Attempts to predict dissipation range onset using simple, parallel-propagating wave theory failed. Obliquely propagating kinetic Alfvén waves were discussed as one possible explanation for the observations.

Figure 1 is an example of the power spectrum of IMF fluctuations at 1 AU discussed in Paper 1. At 0.24 Hz, the spectrum "breaks" from a $\nu^{-1.67}$ power law inertial range to a $\nu^{-2.91}$ dissipation range. We call this frequency the spectral break frequency ν_{bf}. We contend that the steepened spectrum marks the onset of dissipation. The spacecraft spintone can be seen at 0.33 Hz along with at least six harmonics. The flattening of the spectrum at the highest frequencies is due to an undetermined noise source on the spacecraft. (See Paper 1 for a more detailed discussion of this problem.)

We use 83 such 1-hour intervals of Wind data in this paper; the 33 intervals of quiet solar wind data used in Paper 1, and 50 hours from January 9–11, 1997, containing a large coronal mass ejection (CME) and imbedded magnetic cloud [*Leamon et al.*, 1998b]. These 83 events cover a wide range in all solar wind parameters (B, β_p, V_{SW}, Θ_{BV}) and ν_{bf}. (Thermal particle measurements are from the SWE instrument [*Ogilvie et al.*, 1995] on board Wind.) In particular, the angle between the mean field and the solar wind velocity vector varies over the range $9.1° \leq \Theta_{BV} \leq 87.1°$. The spectrum shown in Fig-

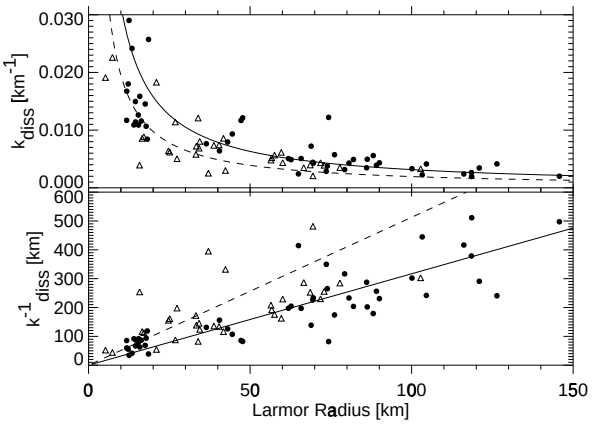

FIGURE 2. Two scatterplots showing inverse relationship between the observed frequency marking the onset of the dissipation range and the Larmor radius for a thermal proton. The solid line in each case corresponds to the best-fit straight line of the bottom panel, namely $k_{diss}^{-1} = (3.172 \pm 0.152) R_L$, and the dashed curve corresponds to the best-fit hyperbola of the top panel, $k_{diss} = (0.195 \pm 0.012) R_L^{-1}$. Observations in the quiet solar wind dataset used by Paper 1 are shown as triangles, and those from the January 1997 CME (see *Leamon et al.* [1998b] for more details) are represented by circles.

ure 1 is fairly typical of 1 AU observations and the ambient plasma parameters of the period are also typical for 1 AU.

Figure 2 shows two representations of the relationship between the Larmor radius for thermal protons R_L and the dissipation wavenumber $k_{diss} \equiv 2\pi\nu_{bf}/V_{SW}$. Dissipation sets in when k^{-1} scales are of the order of the proton Larmor radius, without regard for Θ_{BV}. A slab geometry would introduce an extra factor of $\cos\Theta_{BV}$ into the dependence of k_{diss} on R_L, which is manifestly absent in Figure 2. The fact that the particular choice of a slab geometry fails to organize the observations was previously demonstrated by *Leamon et al.* [1998a, Figure 7]. Figure 2 seems to suggest that there is always a fluctuation that projects onto V_{SW} as R_L to mark the onset of dissipation: the fluctuations are more than just an ensemble of parallel-propagating ("slab") Alfvén waves. What is needed, according to Figure 2, is a more nearly isotropic dissipation mechanism that is associated, at least in part, with cyclotron resonance.

For low-frequency magnetic field fluctuations, cyclotron-resonant dissipation is most effective when the wave vector forms a small angle with the mean magnetic field. Landau damping, either by ions or electrons, favors oblique wave vectors and in the remainder of this paper we will demonstrate that it provides the necessary damping of waves at large propagation angles. In the process we will argue that a significant fraction of the dissipated magnetic energy (about half) is used to heat the ambient thermal electrons; the remainder heats the ions.

This paper is concerned only with the dissipation mechanisms; the rate at which energy is transferred through the inertial range and supplied to the heating mechanisms and the geometry of the spectrum are both beyond the scope of this effort, except in so far as a couple of simple comparisons that can be made at the end of the paper. So as not to bias this analysis we will assume an isotropic spectrum of known energy level and allow future efforts to refine this assumption when considering specific models for the spectrum and spectral transfer of energy.

3 KINETIC ALFVÉN WAVES

The kinetic Alfvén wave (KAW) can be viewed as a coupling of the ion-acoustic mode and the Alfvén wave [see, *e.g.*, *Hasegawa*, 1976; *Lysak and Lotko*, 1995; *Hollweg*, 1999]. It was introduced by Hasegawa by including finite Larmor radius effects in the MHD equations. It also undergoes both electron and ion Landau damping through its coupling to the electrostatic mode [*Hasegawa and Uberoi*, 1982]. It produces compressive (parallel) magnetic field fluctuations and has a parallel electric field component. Unlike the magnetosonic mode considered by *Barnes* [1966], the kinetic Alfvén wave experiences Landau damping only at scales comparable to the ion Larmor radius.

Kinetic Alfvén waves have been implicated in a wide variety of geophysical processes from the ionosphere to the solar corona [for an exhaustive list, see *Hollweg*, 1999]. There are a number of reasons why kinetic Alfvén waves provide an interesting model for our problem of solar wind IMF fluctuations: for instance at low wavenumbers, they are mostly transverse, with a minimum variance direction close to $\mathbf{B}_0$ and thus are not inconsistent with the observations of *Belcher and Davis* [1971], even though they are not parallel propagating. As k increases and the solutions approach dissipation-range frequencies, however, this approximation breaks down and the KAW becomes strongly compressive when $k_\perp^{-1}$ is of the order of the ion Larmor radius [*Hasegawa and Sato*, 1989; Paper 1].

As discussed in section 5 of Paper 1, of the three low-frequency, obliquely propagating wave modes,

both the fast magnetosonic wave and the slow-mode wave are heavily damped in a high-β plasma, regardless of wavelength. Observations of the presence of a spectral break, therefore, makes it highly unlikely that these two wave modes can provide an adequate explanation of the observed data. It is a critical assumption that we make in the rest of this paper that all magnetic fluctuation energy is contained in KAWs.

Throughout this paper we will be using KAW dispersion relations calculated via solution of the linearized Maxwell-Vlasov equations without any further approximations or limits, in order to analyze in detail the properties of the KAW in association with the dissipation and damping of IMF fluctuations. We assume single-temperature Maxwellian distributions for both protons and electrons with, unless otherwise stated, $\beta = \beta_p = \beta_e$, where for each species $\beta \equiv 8\pi n k_B T/B^2$.

3.1 Analytic Approximations to the Kinetic Alfvén Wave

Even though numerical calculations are the best method of determining the full KAW dispersion relation, we can consider analytic approximations to it for the purposes of demonstrating the mode couplings. *Hasegawa and Sato* [1989] give the following expression for the dispersion relation:

$$\left(I_0(\lambda_i)e^{-\lambda_i} - \frac{\omega^2}{k_\parallel^2 c_s^2}\right)\left[1 - \frac{\omega^2}{k_\parallel^2 V_A^2}\frac{1}{\lambda_i}\left(1 - I_0(\lambda_i)e^{-\lambda_i}\right)\right]$$

$$= \frac{\omega^2}{k_\parallel^2 v_{th,i}^2}\left(1 - I_0(\lambda_i)e^{-\lambda_i}\right), \qquad (1)$$

where $c_s = (k_B T_e/m_i)^{1/2}$ is the ion sound speed with electron temperature, V_A is the Alfvén speed, $v_{th,i}$ is the ion thermal speed, $\lambda_i = k_\perp^2 R_L^2$ and $I_0(\lambda_i)$ is the modified Bessel function of the first kind. Subscript symbols $\perp$ and $\parallel$ refer to the directions perpendicular and parallel to the mean magnetic field, respectively. Equation (1) neglects damping, *i.e.*, ω is only the real part of the frequency. We would like to point out that for a high-β plasma like the solar wind ($\beta \sim \mathcal{O}(1)$), the correction to (1) can be substantial. Nevertheless, (1) clearly shows the coupling of the ion acoustic mode (zero of first parenthesis) and the Alfvén wave (zero of square brackets).

In a low-β plasma, $c_s^2 \ll V_A^2$, the coupling is weak and the dispersion relation for the kinetic Alfvén wave becomes

$$\frac{\omega^2}{k_\parallel^2 V_A^2} = \frac{\lambda_i}{1 - I_0(\lambda_i)e^{-\lambda_i}} + \frac{T_e}{T_i}\lambda_i. \qquad (2)$$

Furthermore, if $\lambda_i \ll 1$, the dispersion relation reduces to

$$\omega^2 = k_\parallel^2 V_A^2\left[1 + k_\perp^2 R_L^2\left(\frac{3}{4} + \frac{T_e}{T_i}\right)\right] \qquad (3)$$

Equations (1)–(3) are all from *Hasegawa and Sato* [1989].

3.2 Calculated Properties of the Kinetic Alfvén Wave

Figure 3 shows the dispersion relations we compute for waves propagating at various angles to the mean magnetic field and for the specific value of $\beta = 0.5$. From the wave frequency (top) panel, we can see that dispersion is fairly independent of propagation direction until $\theta_{kB} \gtrsim 60°$, due to the $\cos\theta_{kB}$ dependence of kinetic Alfvén waves. The parallel-propagating wave has the greatest decay rate (bottom). However, the decay rate for oblique propagation is of comparable magnitude until large oblique angles ($\theta_{kB} \gtrsim 60°$). This "quasi-isotropic" dissipation is in agreement with the implications of Figure 2.

Our codes calculate the dispersion relation via the contributions of electrons and protons to the dispersion tensor D. We calculate the ratios of the fluctuating electric field components $\delta\mathbf{E}$ of the wave via the relation $\mathsf{D}(\mathbf{k},\omega)\cdot\delta\mathbf{E}(\mathbf{k},\omega) = 0$ [*e.g.*, *Gary*, 1993], and then $\delta\mathbf{B}$, via Maxwell's equations. Figure 4 shows the ratio of these fluctuating $\delta\mathbf{B}$ components, along with the dispersion relation.

We terminate each calculation in Figure 4 when $\gamma/\omega = -0.5$; at this point the wave is critically damped, and beyond this, the wave can no longer be viewed as propagating.

From $\nabla\cdot\mathbf{B} = 0$ we have $\delta B_x/\delta B_z = -\cot\theta$ (we assume that the wave propagates in the x–z plane), which is a constant for a given propagation direction. At low values of k, $|\delta B_y/\delta B_z|$ is large, demonstrating the transverse nature of the KAW; as k increases, the KAW becomes more compressive, and this ratio decreases towards unity. Rather than showing ratios of the components of $\delta\mathbf{E}$, we show in Figure 4 the quantity $|\mathbf{k}\cdot\delta\mathbf{E}|/|\mathbf{k}\times\delta\mathbf{E}|$, which may be viewed as a proxy to the ratio of Landau to cyclotron damping. We see that $|\mathbf{k}\cdot\delta\mathbf{E}|/|\mathbf{k}\times\delta\mathbf{E}|$ increases for increasingly off-axis propagation directions.

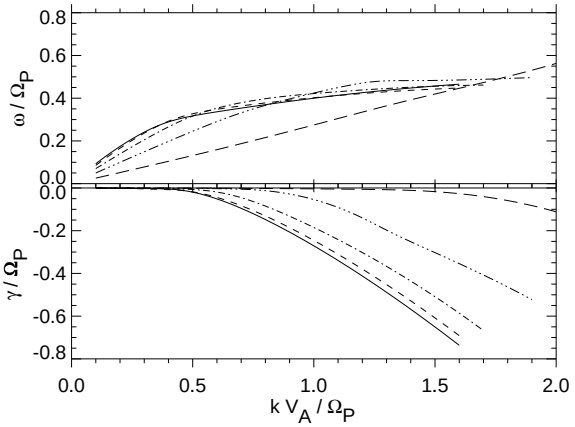

FIGURE 3. Dispersion relations for kinetic Alfvén waves propagating at various angles to the mean magnetic field. The wavenumber k, real frequency ω, and damping rate γ are all scaled to dimensionless units. (The quantity kV_A/Ω_p is identically equivalent to kc/ω_{pi}, as is sometimes used by other authors.) The key to the lines is as follows: solid, 15°; dashed, 30°; dot-dashed, 45°; dot-dot-dot-dashed, 60°; long dashed, 75°. All solutions are for $\beta_p = \beta_e = 0.5$.

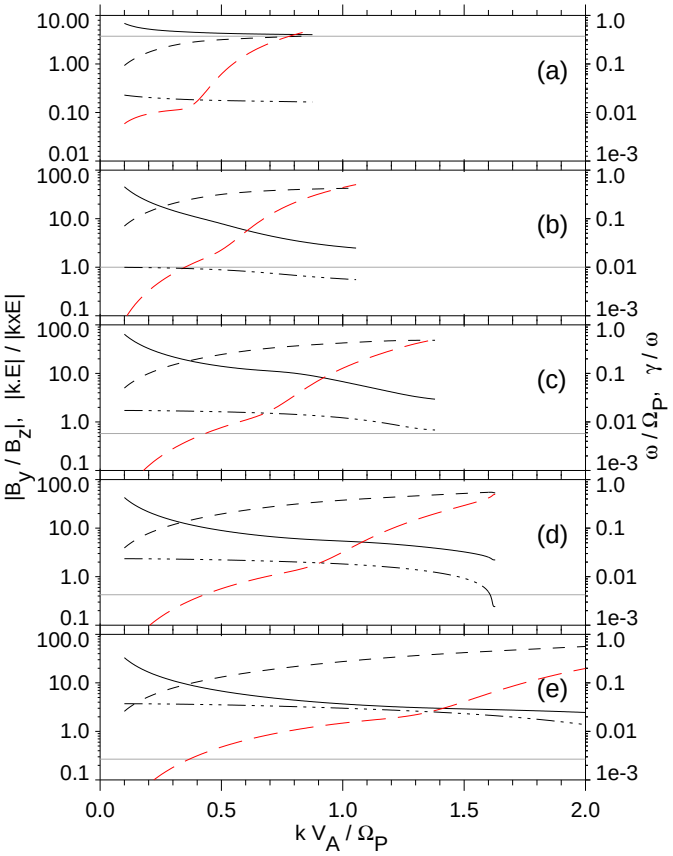

FIGURE 4. A refinement of Figure 3 showing the polarization properties of the wave mode. (a–e) The angle θ_{kB} = 15°, 45°, 60°, 67° and 75°. The solid curve corresponds to $|\delta B_y/\delta B_z|$; the dot-dot-dot-dashed curve, $|\mathbf{k}\cdot\delta\mathbf{E}|/|\mathbf{k}\times\delta\mathbf{E}|$; the dashed curve, ω/Ω_p; and the long dashed curve, γ/ω. The horizontal trace in each panel corresponds to $|\delta B_x/\delta B_z|$, which is a constant for given θ_{kB}.

Various types of damping contribute to the decay rates shown in Figures 3 and 4: ion cyclotron, ion Landau and electron Landau damping, and transit-time magnetic damping. Landau damping and transit-time damping are both due to the $n = 0$ term contribution from the dielectric tensor [*Stix*, 1992]. The $n = 0$ contribution can be either resonant or nonresonant in nature, depending upon the underlying particle and field parameters.

Landau damping and transit-time damping are two distinct physical processes; Landau damping is due to the interaction of the particles with the wave electric fields, and is mainly electrostatic, whereas tranist-time damping is due to the interaction of the particles with the parallel magnetic field δB_z (the compressible perturbation) and is electromagnetic in nature. In general, it is extremely difficult to separate the contributions from various damping processes (since both the $n = 0$ and ± 1 terms contribute significantly to the dispersive properties of the KAW). However, Figure 4 does indicate that $\delta B_z \ll \delta B_y$ for all angles at low-to-moderate wavenumber, which suggests that transit-time magnetic damping might not be as important as other damping processes in this parameter regime. (The magnetosonic wave is, by its more compressive nature, therefore, much more susceptible to transit-time damping than the KAW; however, as mentioned at the start of section 3, the magnetosonic wave damps too quickly to be capable of an adequate explanation of the observed data.)

We can isolate the electron and ion contributions to Landau damping by lowering β_e to very small values; whatever damping is left is due to the protons. We cannot, however, separate and quantify the two contributions of the two ion damping mechanisms. Using solutions such as those shown in Figure 3, we can compute contours of constant γ/Ω_p for a range of β. Figure 5 shows the changes in the contour $\gamma/\Omega_p = -3 \times 10^{-3}$ with changing β_e. For negligible β_e (solid trace), as we move further off-axis we need to go to higher k to find the the same damping rate, as we would expect for cyclotron damping.

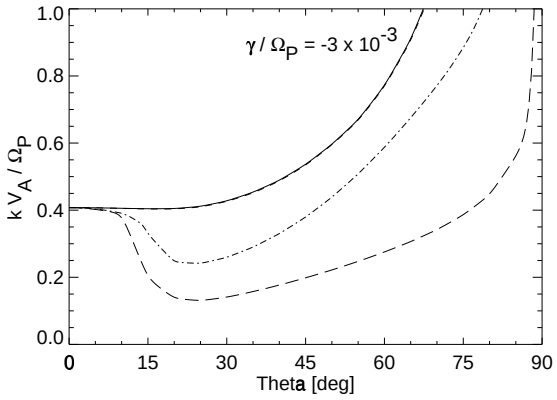

FIGURE 5. Contours of constant γ/Ω_P as a function of increasing β_e. All three contours have $\beta_p = 0.5$, the solid curve is $\beta_e = 10^{-6}$ (so as to virtually remove electron effects from the contour), the dot-dashed curve is $\beta_e = 0.5$, and the long-dashed curve is $\beta_e = 2.5$. Electron effects have very little effect when $\beta_e = 0.01$; such a contour is indistinguishable from the solid curve.

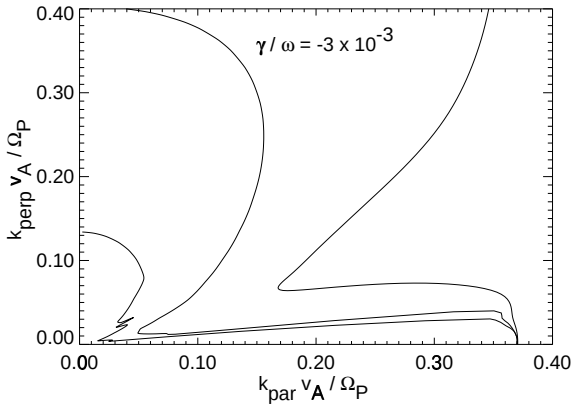

FIGURE 6. Demonstrating that electron resonance effects control the shape of the $\gamma/\omega = -3 \times 10^{-3}$ contour. All three contours have $\beta_p = 0.5$; from the outside in, the values of β_e for the three contours are 10^{-6}, 0.5, and 2.5. The "spikes" seen in the innermost contour at intermediate angles are real; we attribute them to cyclotron effects ($n = 2$, 3, 4), and the rest of the contour is dominated by electron-Landau damping.

The minimum value of k actually occurs at $\theta \sim 15°$, where the two damping mechanisms combine; we can infer from the very shallow nature of the minimum that the cyclotron contribution is greater than that of Landau damping but that some Landau damping occurs. A 4-order of magnitude increase of β_e from 10^{-6} to 10^{-2} produces no clear change in γ, so we conclude that the Landau damping observed in these cases are due to ion Landau damping. As β_e increases further, electron Landau damping increases. Damping is strongest at $\theta \sim 15°$–$30°$, where ion cyclotron damping also contributes, but continues to large angles.

The other feature to note in Figure 5 is that as $\theta_{kB} \to 90°$, $\gamma/\Omega_p \to 0$, and the contours become parallel to the k-axis. The KAW, or, at least, our linear codes, cannot address damping of rigorously 2-D turbulence. However, contours of constant γ/ω are finite at $\theta_{kB} \to 90°$ for 3 of the 4 values of β_e that appear in Figure 5.

It is traditional to examine contours of constant γ/ω as a comparison of the two halves of the solution to the dispersion equation; we show such contours in Figure 6, this time on a $k_\parallel$–$k_\perp$ plot. Figures 5 and 6 show that ion-cyclotron resonance dominates dissipation for small angles, but electron-Landau damping dominates above the cusp.

We can attempt to attribute the origins of the various features of Figures 4 and 5 by looking at contour plots of $|\mathbf{k} \cdot \delta\mathbf{E}|/|\mathbf{k} \times \delta\mathbf{E}|$, as shown in Figure 7. To first order, as θ increases, so does $|\mathbf{k} \cdot \delta\mathbf{E}|/|\mathbf{k} \times \delta\mathbf{E}|$; Landau damping becomes more important. This suggests that the cusp in Figures 5 and 6 is due to the combined effects of cyclotron and Landau resonance that are both efficient when $\theta_{kB} \sim 15°$.

Note also, in Figure 7, that for small values of k in the range $\theta_{kB} = 15°$–$30°$ there is a local increase in $|\mathbf{k} \cdot \delta\mathbf{E}|/|\mathbf{k} \times \delta\mathbf{E}|$ that persists for all values of β_e. We might infer from this a localized enhancement of ion Landau damping, but we cannot verify this, for reasons explained in the following paragraph.

Notice that for almost all points in $\mathbf{k}$ space, $|\mathbf{k} \cdot \delta\mathbf{E}|/|\mathbf{k} \times \delta\mathbf{E}|$ decreases with increasing β_e. This is somewhat counterintuitive, as we would expect the electron damping strength (all due to Landau resonance) to increase with increasing β_e. This effect is especially pronounced in the two "wells" at $\theta \sim 75°$ in Figure 7c ($\beta_e = 2.5$). We may be able to explain this behavior as follows: as β_e increases (relative to fixed β_p) the enhanced damping affects the dispersion relation $\omega(\mathbf{k})$, as suggested by (2) and (3), which in turn causes $|\mathbf{k} \cdot \delta\mathbf{E}|/|\mathbf{k} \times \delta\mathbf{E}|$ to decrease. For this reason, we are not able to separate the contributions of ion Landau and ion cyclotron damping through examination of $|\mathbf{k} \cdot \delta\mathbf{E}|/|\mathbf{k} \times \delta\mathbf{E}|$ alone. Pursuing this goal by other methods (*e.g.*, Taylor expansion of the dispersion tensor $\mathsf{D}(\mathbf{k}, \omega)$) is beyond the scope of the present paper.

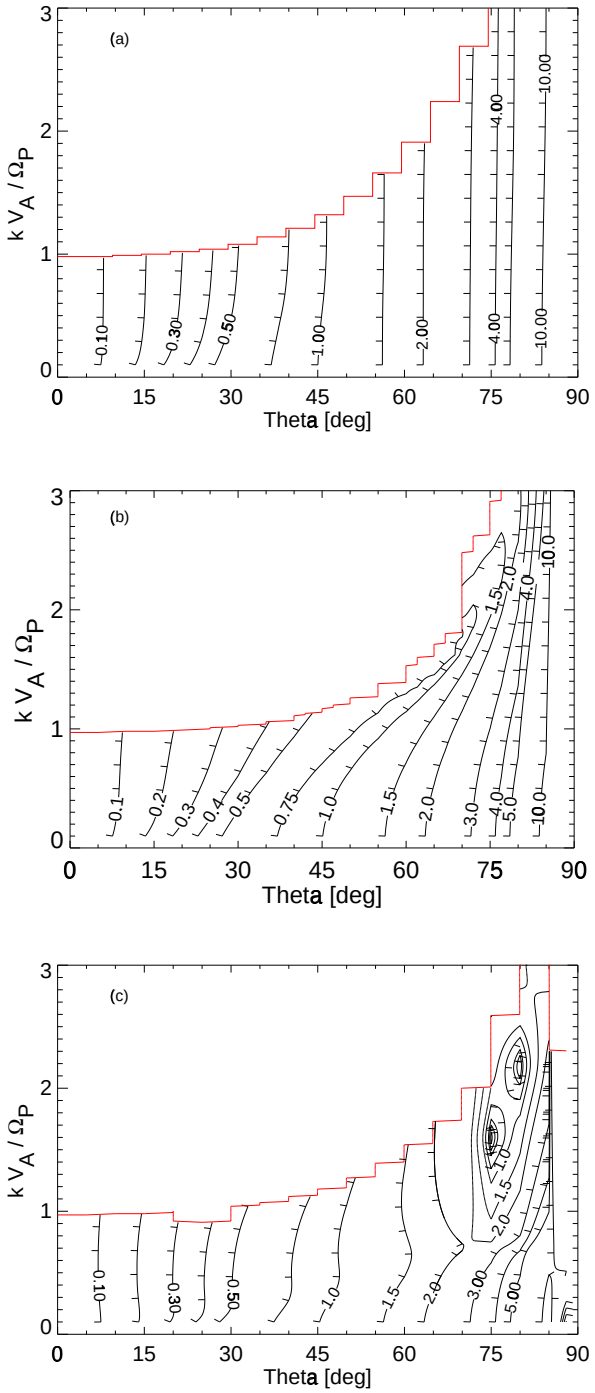

FIGURE 7. Contour plots of $|\mathbf{k}\cdot\delta\mathbf{E}|/|\mathbf{k}\times\delta\mathbf{E}|$ for three different values of β_e: (a) 10^{-6}, (b) 0.5, and (c) 2.5. All three panels have $\beta_p = 0.5$, and the same set of contour values. The stair-stepping lines correspond to where $\gamma/\omega = -0.5$, at which point the wave may no longer be viewed as propagating (see text).

Considering the simple turbulence model of balancing cascade rate with dissipation for left- and right-hand polarized structures [*Leamon et al.*, 1998c] suggests that, as a global average, cyclotron-resonant damping rates are approximately twice the sum of Landau-damping and other, nonresonant damping rates. However, since $\gamma(\mathbf{k})$ varies greatly with increasing k and θ, as we have shown, we cannot say what the relative contributions of ion Landau and ion cyclotron damping are at any particular point in $\mathbf{k}$ space.

To conclude this section we show in Figure 8 contours of γ/Ω_p for a range of β, and in Figure 9 contours of γ/ω. Figure 8 demonstrates compactly the effect on $\gamma(\mathbf{k})$ of k, θ and β. Throughout the range of β, contours of large (negative) γ/Ω_p (the upper contours) follow a nearly positive-definite rise to larger k with increasing θ_{kB}. For the lower contours, where dissipation is less, a greater degree of structure can be seen as the Landau resonances display their variability. If one envisions an established 3-D spectrum that is convected at varying values of θ_{kB}, the variability of the lower contours will lead to changes in the dissipation range onset frequency in what may be a fairly complex manner. Prediction of that onset in the measured reduced spectrum is therefore sensitive on both β and θ_{kB}. We shall show in the section 5 that the onset prediction also depends on Θ_{BV}.

Note that in both Figures 8 and 9, the contours at low θ_{kB} change very little with increasing β. The contours of higher γ/ω are noticeably more independent of θ_{kB} over the whole range of β in Figure 9, *i.e.*, more isotropic than the contours of γ/Ω_p. At the same time, a much higher degree of variability is seen in the lower contours. We argue in the next section that the onset of the dissipation range is determined by these lower, highly variable contours for surprisingly small values of γ/ω.

4 SYNTHESIZED 3-D SPECTRUM

The purpose of the present section is to test how well the observed properties of IMF fluctuation power spectra can be explained by the damping of kinetic Alfvén waves. We have, as a result of the previous two sections, (*i*) a collection of observed reduced power spectra $F(f)$ exemplified by Figure 1; and (*ii*) linear solutions of the KAW stability. On the basis of these solutions, we shall construct a sample 3-D spectrum $E(\mathbf{k})$, and test if the power law and abrupt break can be preserved when this is reduced

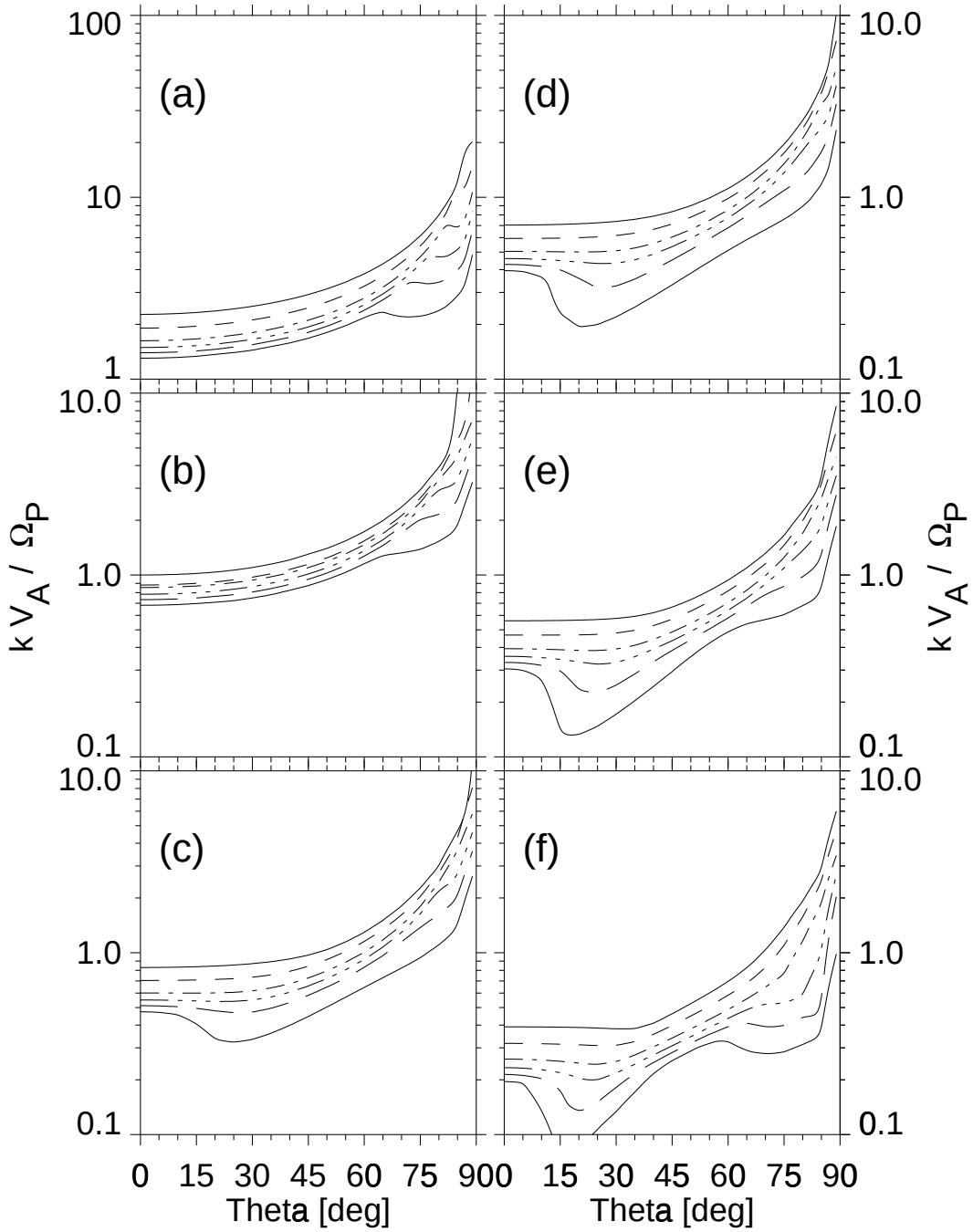

FIGURE 8. Contour plots of constant γ/Ω_p for six different values of β: (a–f) $\beta = 0.01$, 0.1, 0.3, 0.5, 1.0 and 3.0. The six contours are the same for all six panels; from the outside, $\gamma/\Omega_p = -0.1$ (solid), -0.05 (dashed), -0.02 (dot-dashed), -0.01 (dot-dot-dot-dashed), -5×10^{-3} (long-dashed) and -2×10^{-3} (solid). In all cases, both the wave frequency ω and the growth (damping) rate γ approach zero as the wave propagation direction becomes perpendicular to the mean field.

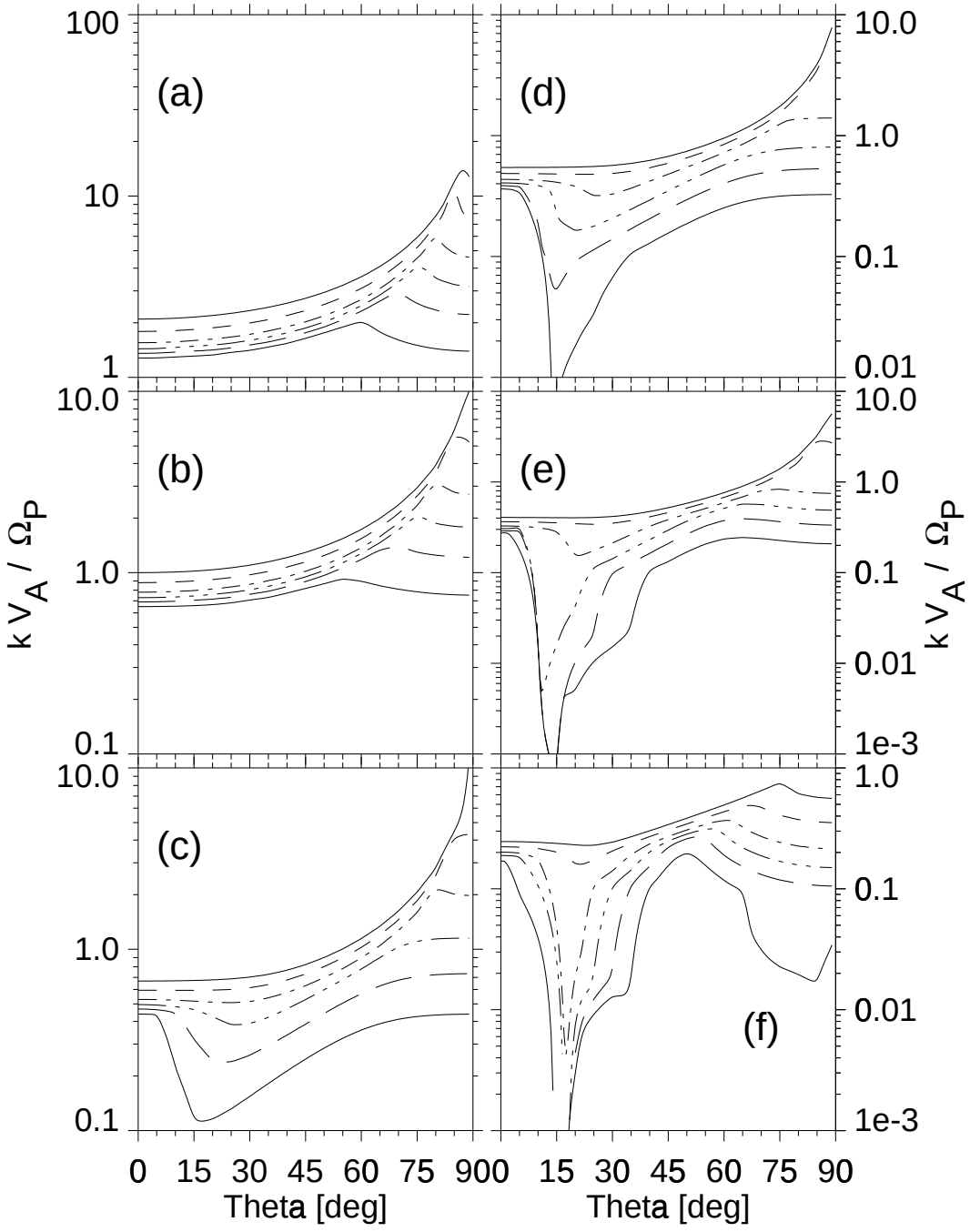

FIGURE 9. Same as Figure 8, but contours of constant γ/ω. The numerical values of the contours are the same as Figure 8.

to $F(f)$. In this way we obtain a 3-D spectrum that is consistent with the observations, but not unique.

4.1 Assumptions

We aim to reproduce the spectrum shown in Figure 1. Our synthetic $E(\mathbf{k})$ is azimuthally symmetric about $\mathbf{B}_0$. Taking the whole set of KAW solutions for $\beta = 0.5$ (recall that the observed $\beta_p = 0.48$ for that interval), we assume that dissipation sets in at some contour of constant γ/ω. We choose contours of constant γ/ω rather than constant γ (or, more precisely, γ/Ω_p) for two reasons: (*i*) contours of γ/ω remain finite as $\theta \to 90°$; and (*ii*) γ/ω is more relevant than γ alone for determining the time taken for a wave to decay [*Barnes*, 1966]. Thus

$$E(\mathbf{k}) = E(k,\theta) = \begin{cases} A_0 k^{-11/3} & k < k_* \\ A_0 k_*^{-11/3} (k/k_*)^{-5} & k \geq k_* \end{cases}, \quad (4)$$

where $k_*(\theta)$ defines the contour of γ/ω. $E(\mathbf{k})$ is set up as a 200×181 array, with 200 logarithmically spaced k values between $kV_A/\Omega_p = 5 \times 10^{-4}$ and 21.0, and 181 angles in half-degree steps from zero (parallel) to 90°. The exponents are set at $-11/3$ and -5 so that the reduced one-dimensional power spectrum will have inertial- and dissipation range spectral indices of $-5/3$ and -3 if the spectrum reduces correctly. A_0 is a global scaling factor, and is not a function of θ; the only anisotropy present in the assumed spectrum is that which arises from the $k_*(\theta)$ contour.

The values of $k_*(90°)$ and $k_*(89.5°)$ are set equal to $k_*(89°)$. Our codes cannot determine a dispersion relation for $\theta = 90°$ (indeed, a propagating wave *per se* does not exist). We can see from the flat nature of the contours at large angles in Figure 9 that this is a reasonable approximation to make. Since waves cannot propagate at $\theta = 90°$, our model cannot address rigorously 2-D fluctuations, but may be able to damp nearly, but not perfectly, perpendicular to $\langle \mathbf{B} \rangle$. We do obtain propagating solutions for θ as high as 89°.

We acknowledge the *ad hoc* nature of the assumption that $k_*(\theta)$ is defined by the contour $\gamma/\omega =$ constant. To the extent that hydrodynamic turbulence theory predicts the onset of a dissipation range spectrum when dissipation becomes competitive with the cascade of energy from larger spatial scales [*Batchelor*, 1953], we are ignoring half of the problem by predetermining the onset of the dissipation range spectrum according to dissipation dynamics alone.

There are several reasons that partially justify our assumption: First, the linear decay rates, γ, computed in the previous section increase more rapidly after the initial onset of dissipation than the νk^2 form of hydrodynamics. In hydrodynamics, dissipation responds to increases in the energy cascade rate by moving the onset of the dissipation range spectrum to larger k until the balance between energy cascade and dissipation is reestablished. Such a response in this system is unlikely to result in a significant shift in k_{diss} due to the rapidly increasing functional form of γ.

Second, *Kraichnan* [1965] postulates that the timescale governing the cascade of energy in the MHD inertial range is $\tau \sim 1/kV_A = 1/\omega$. If we balance dissipation timescales against cascade timescales, $\gamma/\omega = \gamma\tau$ becomes a natural measure for the increased importance of dissipation. It is not the only measure, but it is one. Admittedly, most of the inertial range spectra in our set of observations are more nearly comparable to the $k^{-5/3}$ prediction of *Kolmogoroff* [1941] than the $k^{-3/2}$ prediction of Kraichnan. Even so, we feel this lends some support to our assumption to scale the dissipation rate at the onset of dissipation with Kraichnan's prediction for the timescale governing spectral transfer, especially as the cascade in the Kolmogoroff picture depends on energy at low k, that are poorly determined, if at all, by our 1-hour samples of the solar wind.

Last, we note that the comparisons of the latter half of this paper are intended only to illustrate the likely role of kinetic Alfvén waves in the evolution of the dissipation spectrum. We acknowledge the extreme complexity of building a turbulence model that accounts for anisotropic spectral transfer, the dissipation of 2-D fluctuations and the dependence of both upon ambient plasma parameters. We offer this simple analysis as a reasonable beginning.

4.2 Reduction to Frequency Spectrum

Having constructed our synthetic 3-D spectrum $E(\mathbf{k})$, we now reduce it to a Doppler-shifted frequency spectrum according to

$$F(f) = \int E(\mathbf{k})\, \delta\left(\frac{1}{2\pi}\left(\mathbf{k}\cdot\mathbf{V}_{SW} + \omega(\mathbf{k})\right) - f\right) d\mathbf{k} \quad (5)$$

where $\omega(\mathbf{k})$ is the real part of the wave frequency determined from the linear Vlasov-Maxwell solutions, $\delta(\ldots)$ is the Dirac delta function, f is the spacecraft-frame frequency, and for $\mathbf{V}_{SW}$ we take the observed

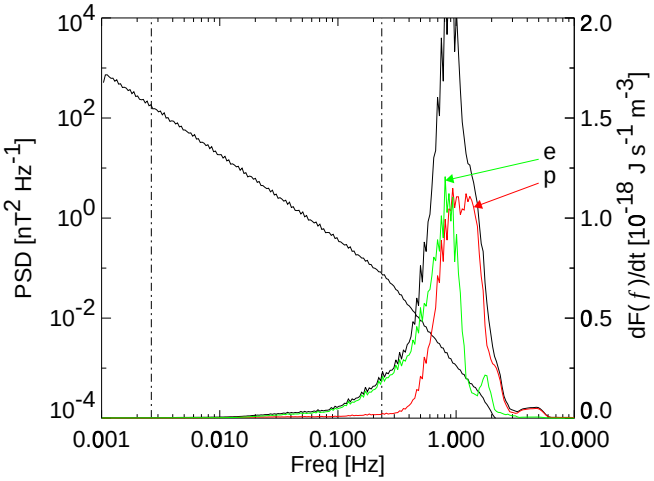

FIGURE 10. Synthetic power spectrum of kinetic Alfvén waves (left-hand scale) and heating rate $dF(f)/dt$ as a function of frequency. The total heating rate, which is the sum over all of the 250 logarithmically spaced frequency bins used, is 6.36×10^{-17} J s^{-1} m^{-3}. Under the heating rate curve are the electron and proton contributions, at slightly lower and higher frequencies, respectively.

solar wind velocity for the interval in question. At this point the constant A_0 in (4) is set by trial-and-error so as to match the observed inertial range amplitude of the interval shown in Figure 1. The results of this reduction are shown on the left-hand scale of Figure 10. We can see that the spectrum does indeed reduce correctly to $-5/3$ and -3 power laws, and that the break in the spectrum is almost exactly reproduced. The two vertical lines in Figure 10 correspond to the observed spectral break at 0.235 Hz and the lowest frequency in Figure 1, 2.7×10^{-3} Hz. The break contour used in computing Figure 10 is $\gamma/\omega = -3 \times 10^{-3}$.

4.3 Heating

Having successfully tested our synthetic 3-D spectrum's ability to reproduce the break in the reduced frequency spectrum, we can now calculate the rate at which damping of kinetic Alfvén waves with this spectral form heats the background plasma.

The heating rate (in SI units) is given by

$$\dot{Q} = \frac{1}{2\mu_0} \int 2E(\mathbf{k})\gamma(\mathbf{k}) d\mathbf{k} \qquad (6)$$

where $\gamma(\mathbf{k})$ is the imaginary part of the wave frequency. Evaluating this integral for the $E(\mathbf{k})$ computed above gives $\dot{Q} = 6.36 \times 10^{-17}$ J s^{-1} m^{-3}.

By including a Dirac delta function similar to that in (5), we can see how this heating is distributed in frequency. This is shown in the second trace and right-hand scale of Figure 10. There is some heating in the inertial range of the spectrum, but the bulk of the heating is at dissipation range frequencies, peaking at $\simeq 1$ Hz.

Given our earlier discussion on how electrons and protons affect the contours of constant γ/ω, it is of interest to see how much of the energy dissipated goes to heating electrons and how much goes to heat protons. To do so, we take our solutions of $\gamma(\mathbf{k})$ for $\beta_e = 10^{-6}$, thereby effectively removing all electron-resonant damping. Using the same $E(\mathbf{k})$, we recompute the heating rate of protons only, which is 3.66×10^{-17} J s^{-1} m^{-3} or 57.5% of the total. The electron contribution is never determined by itself; it is taken to be the difference of total and proton heating. The two heating distributions as functions of frequency are also shown in Figure 10. The proton contribution is broader, peaks at a higher frequency, and it is the electrons alone that contribute to inertial range heating.

4.3.1 Differing electron and proton temperatures

As a demonstration of electron effects, we have also investigated increasing β_e and with it the damping rates for oblique propagation. Again, keeping $\beta_p = 0.5$, we increased β_e to 2.5. A new $E(\mathbf{k})$ was determined using the newly computed KAW dispersion solutions, but keeping the same critical value of γ/ω for the spectral break contour; *i.e.*, using the innermost contour of Figure 6. Figure 11 shows the frequency spectrum $F(f)$ and heating rate $\dot{Q}$ based on this elevated β_e.

The break in the new $F(f)$ is now at about 0.09 Hz, despite the fact that the proton-dominated parallel lobe of Figure 6 is virtually unchanged with increased β_e. We might reasonably expect therefore that the parallel lobe plays little role in determining the location of the spectral break in this example, which is controlled mostly by: (*i*) electron, rather than proton effects; and (*ii*) dissipation at moderate to large angles of propagation. This goes against the commonly held (and indeed used in Paper 1) intuition that proton cyclotron resonant effects alone determine the location of the spectral break.

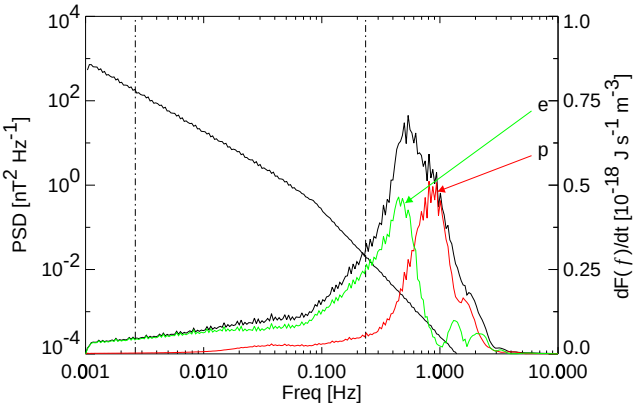

FIGURE 11. Same as Figure 10 using $\beta_e = 2.5$, $\beta_p = 0.5$. The spectral break frequency is underestimated by a factor of about 3. The total heating rate is now 4.09×10^{-17} J s^{-1} m^{-3}, of which the protons contribute only 39.8%. Note the large amount of heating at inertial range frequencies due to the electrons.

4.3.2 Solar wind temperature profile

The observed radial solar wind proton temperature profile would be expected to fall as $T_p \sim R^{-4/3}$ if the solar wind were to cool adiabatically as it expands out into the heliosphere. However, the observed Voyager 1 and 2 profile from 1–43 AU falls as $T_p = T_0 R^{-1/2}$ [*Richardson et al.*, 1995], much more slowly than adiabatic. *Gazis and Lazarus* [1982] fitted the data from 1–10 AU and found a $T_p \sim R^{-0.7}$ dependence. In either case there must be, therefore, *in situ* heating of the solar wind. The equation of solar wind temperature evolution [*Williams et al.*, 1995, their (2)] is

$$\frac{dT_p}{dr} + \frac{4}{3}\frac{T_p}{r} = \frac{2}{3}\frac{\dot{Q}}{V_{SW} n k_B}, \qquad (7)$$

where n is the local solar wind number density and k_B the Boltzmann constant. When no *in situ* heating occurs, $\dot{Q} = 0$, and an adiabatic temperature profile results. We can compare our KAW-calculated ion heating rate (57.5% of $\dot{Q}$), to the value required to balance the two sides of (7).

If we take the observed data to fall as $T_p \sim R^{-a}$, then the excess heating (left-hand side of (7)) at 1 AU is $\left[\frac{4}{3} - a\right] T_0$ K AU^{-1}. *Richardson et al.* [1995] took T_0, the temperature at 1 AU, to be 3.8×10^4 K. For our exemplary period, we find the proton temperature gradient excess at 1 AU, derived from $\dot{Q}$ via the right-hand side of (7), to be 1.10×10^5 K AU^{-1}, which is 3.5 times greater than required if we take the Richardson *et al.* values for a and T_0, or only 1.1 times greater than required if we take the observed local temperature for the 1-hour interval, $T_0 = 1.2 \times 10^5$ K. The overestimates become worse if we take the *Gazis and Lazarus* [1982] profile, or any other profile that falls faster with distance than $R^{-1/2}$.

One might argue that those measurements further from the sun have more weight in determining the power law indices for the Voyager radial temperature profile, and as such, the observed $T_p = T_0 R^{-1/2}$ profile is less applicable at 1 AU. *Freeman* [1988] uses Helios data from 0.3 to 1 AU and finds good power-law temperature dependence inside 1 AU. Freeman separates his data according to solar wind speed and finds that the power law index decreases with increasing solar wind speed, while the temperature at 1 AU increases. At very low wind speeds, $V_{SW} < 300$ km s^{-1}, there is almost no implied heating excess. For solar wind speeds in the range $500 < V_{SW} < 600$ km s^{-1}, such as is the case in our exemplary period, Freeman fits a $T_p = 1.3 \times 10^5 R^{-0.826}$ K power law, which implies that the calculated KAW heating is 1.7 times greater than is required to match Freeman's power law.

We believe that these results within a factor of 3 represent acceptable agreement, given the simple nature of our theory and the inherent variability of the solar wind. Indeed, the assumption, as made by *Richardson et al.* [1995], of a single power law temperature profile for all heliocentric distances is by no means certain. A power law is scale invariant, and as such will not be an applicable approximation if new physics becomes important at a specific scale, as is the case for pickup ions beyond about 10 AU. At large heliocentric distances, pickup ions are believed to contribute, if not dominate, the heating through the cascade of ion-excited wave energy [*Williams et al.*, 1995; *Zank et al.*, 1996; *Matthaeus et al.*, 1999], which causes the radial temperature profile to be flatter than it otherwise would. At the inner extremes of Helios' orbit the temperature profile would deviate from adiabatic for another reason, namely the (fast) damping of initial-condition waves [*Tu*, 1988; *Marsch*, 1991] and the slow spectral transfer of energy due to high cross helicity [*e.g.*, *Dobrowolny et al.*, 1980; *Grappin et al.*, 1982, 1983; *Roberts et al.*, 1987b].

4.3.3 Turbulent cascade rate

The one final test we can do with our calculated dissipation rate is to compare it to the turbulent cascade rate ε inferred from the observed inertial range power spectrum (Figure 1). We would expect approximate equality between the two; in the turbulence picture of fluctuations, the rate at which energy enters the dissipation range is balanced by the rate at which it is dissipated and heats the background plasma. For the sake of ease of comparison with previous works in this field, where ε is expressed in cgs units (ergs g^{-1} s^{-1}), we will scale our calculated dissipation rate to these units. Taking the total heating rate (both proton and electron contributions from our synthetic KAW spectrum), we find $\dot{Q} = 8.38 \times 10^7$ ergs g^{-1} s^{-1}.

In inferring ε from the observed power spectrum we will follow the approach of *Coleman* [1968], although we shall correct the slight and subtle error that he introduced. Coleman used the magnetohydrodynamic formulation of *Kraichnan* [1965] to calculate ε: the omnidirectional inertial-range spectrum of turbulent kinetic energy (per unit mass) is

$$E(k) = A(\varepsilon V_A)^{1/2} k^{-3/2}, \tag{8}$$

where V_A is the Alfvén velocity and A is a numerical constant. We shall also consider the hydrodynamic formulation of *Kolmogoroff* [1941]:

$$E(k) = C\varepsilon^{2/3} k^{-5/3}. \tag{9}$$

The two numerical constants A and C can be linked by the relation $A = C^{3/4}$ [*Matthaeus and Zhou*, 1989]. Taking $C = 1.6$ [*Batchelor*, 1953] gives $A = 1.42$.

The $E(k)$ term in (8) and (9) is an omnidirectional spectrum, whereas what we observe in Figure 1 is a reduced spectrum. From Batchelor's equation (3.4.17) and after a few lines of algebra, the two can be related by

$$E^r(k) = \int_k^\infty \frac{E(k')}{k'} dk'. \tag{10}$$

For a power law form $E(k) \sim k^{-\alpha}$, we have $E^r(k) = \alpha^{-1} E(k)$.

So, in the Kraichnan formulation we have

$$E^r(k) = \frac{2}{3} E(k) = \frac{2}{3} A \left(\varepsilon V_A\right)^{1/2} k^{-3/2},$$

which upon rearranging gives

$$\varepsilon = \left(\frac{2}{3}A\right)^{-2} V_A^{-1} \left[E^r(k)\right]^2 k^3.$$

The frequency spectrum in Figure 1, denoted as $F(f)$, must contain the same spectral power in range df as $E^r(k)$ contains in range dk. Therefore $fF(f) = kE^r(k)$. We can also substitute $k = 2\pi f / V_{SW}$, leading us to our final expression for ε:

$$\varepsilon = \frac{2\pi}{V_A V_{SW}} \left(\frac{2}{3}A\right)^{-2} \left[F(f)\right]^2 f^3. \tag{11}$$

Remembering that $F(f)$ must be scaled to velocity (Alfvén) units, and taking the geometric mean over the 370 spectral estimates in the range 0.003–0.1 Hz, we find that $\varepsilon = 5.15 \times 10^6$ ergs g^{-1} s^{-1}, which is 16 times smaller than the KAW dissipation rate (for proton and electron heating combined).

Repeating the same procedure for the Kolmogoroff ($k^{-5/3}$) formulation gives

$$\begin{aligned} \varepsilon &= \frac{2\pi}{V_{SW}} \left(\frac{3}{5}C\right)^{-3/2} \left[F(f)\right]^{3/2} f^{5/2} \qquad (12) \\ &= 1.47 \times 10^8 \text{ ergs g}^{-1} \text{ s}^{-1}, \end{aligned}$$

which is only 1.75 times larger than the KAW dissipation rate. Given that the observed spectral slope of the interval in Figure 1 is -1.67, we feel that the Kolmogoroff-derived result has greater validity than the Kraichnan result.

For completeness, we could also try to compare our dissipation rate with the simple hydrodynamic expression $\varepsilon = u^3/\ell$ [*Batchelor*, 1953], where u is the rms fluctuation speed and ℓ is the correlation scale. However, the correlation scale at 1 AU is typically longer than can accurately be determined from 1 hour of data, so we cannot put significant trust in the resulting value of ε.

5 PREDICTION OF SPECTRAL BREAK FREQUENCY

We can see from Figure 10 how well our model of a 3-D spectrum of kinetic Alfvén waves does at predicting the spectral break frequency, given a judicious choice of γ/ω. What remains to be seen is how well the model works for all the intervals we have studied. The method used to produce Figure 10 that consists of first calculating a k–θ contour for each interval (with the observed β) and each value of γ/ω, and constructing a fully 3-D $E(\mathbf{k})$ to be reduced to a frequency spectrum is rather labor-intensive. Instead, we take an array of values of k lying on contours of constant γ/ω indexed by β and θ and interpolate between them for the precise value of β for the interval in question. For the purposes of demonstration,

we assume that $\beta_e = \beta_p$ and compare the observed break frequency with the prediction derived from the observed β_p.

We adopt a simplified method of performing the frequency reduction shown in Figures 10 and 11. For each of the intervals in our data set, we determine the wavevector lying on the spectral break contour of constant γ/ω for which $\mathbf{k} \cdot \mathbf{V}_{SW}$ is maximum and Doppler shift the frequency corresponding to this $\mathbf{k}$ (read off the appropriate dispersion relation) into the spacecraft frame to be the KAW-predicted break frequency marking the onset of dissipation. The justification for this "maximum projection" argument is as follows: there are a range of wave vectors $\mathbf{k}$ that Doppler shift to the same spacecraft frame frequency f. (Imagine a top-left to bottom-right stripe perpendicular to $\mathbf{V}_{SW}$ on Figure 6.) Some of the wave vectors in this stripe are "outside" the contour, and as such have very little energy (since the dissipation spectrum falls steeply outside the break contour). However, other wave vectors are still "inside" the contour, and have energy-containing inertial range spectra. Those wave vectors whose spectra are already dissipative are hidden by those that are not yet dissipative. Only when a spacecraft-frame frequency is chosen for which no more inertial range energy is left in any 3-D wave vector can the reduced spectrum demonstrate the dissipative form. This occurs when $\mathbf{k} \cdot \mathbf{V}_{SW}$ is maximum along the contour of constant γ/ω. This simple shortcut has been tested against the more detailed analyses of the previous section and verified.

We choose a single value of γ/ω to define the spectral break contour for all intervals in our data set. The value chosen to define the γ/ω contours is varied by trial-and-error until the best-fit straight line through the data has unit slope. The left-hand panel of Figure 12 shows the observed break frequency versus the predicted value using the best-fit value $\gamma/\omega = -0.01$. Each point is calculated from the observed β_p for the corresponding interval in the data set.

Although the best-fit straight line, $y = (-0.043 \pm 0.079) + (1.025 \pm 0.108)x$, is plotted, we do not believe that this line truly represents the data. The January 1997 magnetic cloud data (open circles) clearly form a separate population from the undisturbed solar wind data, and these points affect the slope and intercept of the best-fit straight line. The best-fit line through all the data is clearly not the best fit to the solar wind data points.

According to *Leamon et al.* [1998b], the geometry of magnetic fluctuations is much more two-dimensional in a magnetic cloud, so we must question the validity of our model of obliquely propagating kinetic Alfvén waves on the grounds that a highly collapsed 2-D geometry may exhibit behaviour that lies beyond the linear KAW dispersion relations. We reject the validity of Figure 12a for a second reason: the angle between the mean field and the wave vector $\mathbf{k}$ for which $\mathbf{k} \cdot \mathbf{V}_{SW}$ is maximum is consistently in the range 60°–80°. (There are only four events which are best modelled by "slab" waves determined by ion cyclotron damping, *i.e.*, $\theta_{kB} \lesssim 10°$.) As we have shown in section 3, at these angles electron Landau damping and thus β_e dominates the shape of the contour. It would make sense then if we use β_e rather than β_p to predict the onset of the dissipation range. This is precisely what is done to produce the right-hand panel of Figure 12: the procedure described above is repeated, but the observed β_e is used instead of β_p in interpolating between the different contours of γ/ω derived from the numerical solutions of the dispersion relation. There is far less scatter of the points around the best-fit straight line of $y = (0.099 \pm 0.047) + (1.041 \pm 0.104)x$, which also corresponds to the contour $\gamma/\omega = -0.01$. Again, the angle θ_{kB} for which $\mathbf{k} \cdot \mathbf{V}_{SW}$ is maximum is consistently in the range 60°–80°.

We acknowledge that the data violate the assumption that $\beta_e/\beta_p = 1$, which was used in producing both panels of Figure 12 and we admit the inherent implication that nonunit β_e/β_p affects the damping rate. However, we have shown in section 3.2 (Figure 6) that β_e-dependent resonances control the shape of the γ/ω contour at angles above $\sim 30°$, and proton effects dominate at less oblique angles. Given, therefore, the further observation that the last wave vectors to damp are in the electron-dominated region, we can ignore proton effects and nonunit β_e/β_p in calculating the spectral break frequency.

For the record, we note in the regular solar wind intervals used to generate Figure 12, β_e was, on average, higher than β_p: $\langle\beta_e\rangle = 0.938 \pm 0.564$, $\langle\beta_p\rangle = 0.664 \pm 0.407$, and $\langle\beta_e/\beta_p\rangle = 1.833 \pm 1.406$. The distribution of $\langle\beta_e/\beta_p\rangle$ is decidedly not normal, with large skewness and kurtosis moments.

Thus the conclusion of this section is that it appears that β_e and electron Landau damping control the onset of the IMF dissipation range at spatial scales comparable to the ion gyroradius. At the same time, the waves become more compressive and have greater fluctuations in $|\mathbf{B}|$, as is seen in the observations [see *Leamon et al.*, 1998a, Figures 3 and 4]. These characteristics are consistent with the onset of electron Landau damping and the compressible nature of the KAW at the scale of the ion gyroradius.

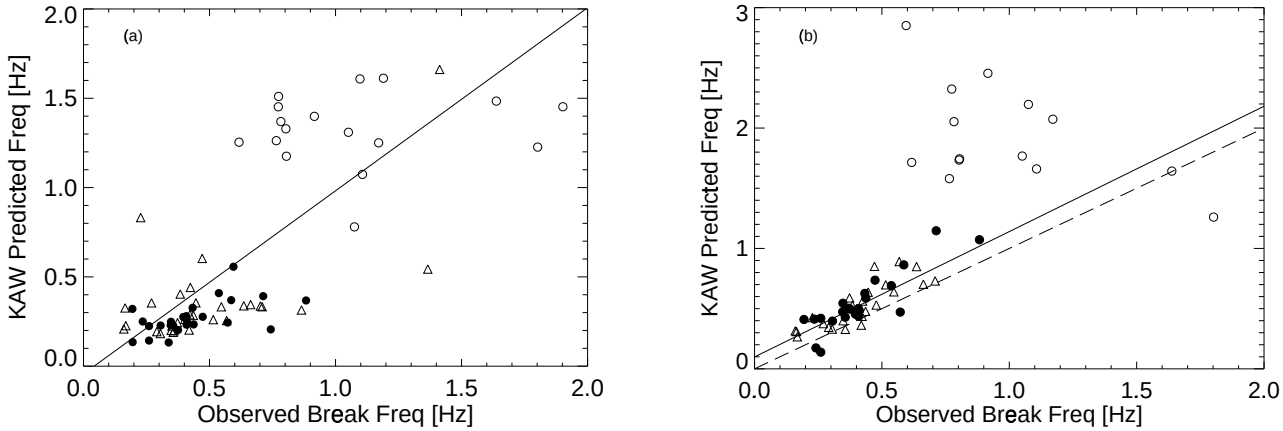

FIGURE 12. Plots of KAW-predicted spectral break frequency against observed break frequency. (a) Best-fit value of $\gamma/\omega = -0.01$, derived from the observed β_p. As in Figure 2, quiet solar wind observations are shown as triangles, and January 1997 observations are circles. Open circles correspond to observations inside the magnetic cloud and filled circles correspond to solar wind observations before and after the CME. The solid line is best-fit straight line, $y = (-0.043 \pm 0.079) + (1.025 \pm 0.108)x$. (b) Using β_e instead of β_p to characterize the observations produces much tighter results. The solid line is the best-fit straight line through the data, excluding the magnetic cloud observations, $y = (0.099 \pm 0.047) + (1.041 \pm 0.104)x$, also corresponding to the contour $\gamma/\omega = -0.01$, and the dashed line is $y = x$. There are fewer data points on this panel because electron plasma data are not available for all the the intervals studied.

Also, paradoxically, β_e influences the heating rate of protons, as shown in section 4.3.1.

6 SUMMARY AND DISCUSSION

The object of this paper has been to examine the damping properties of kinetic Alfvén waves, and to test if an ensemble of such waves can account for the observed features of the power spectrum of IMF fluctuations at 1 AU.

For values of β typically found in the solar wind at 1 AU, contours of constant γ/ω on a $k_\parallel$–$k_\perp$ plot have a two-lobed form. The parallel lobe, for angles $\lesssim 15°$, is dominated by proton cyclotron resonance; and the second lobe $\gtrsim 30°$ is controlled by electron Landau resonance.

We constructed candidate spectra to represent the unmeasurable 3-D spectrum $E(\mathbf{k})$ that were consistent with the observed reduced spectra $F(f)$. $E(\mathbf{k})$ was defined with a spectral break along a contour of constant γ/ω. For the appropriate contour, $\gamma/\omega = -3 \times 10^{-3}$, the reduced frequency spectrum $F(f)$ has a spectral break at the same frequency as in the observed power spectrum. This is a surprisingly small value. For the dispersion relation of $\beta = 0.5$, $\gamma/\omega = -3 \times 10^{-3}$ occurs at $kV_A/\Omega_p = 0.2$ when $\omega/\Omega_p = 0.14$. The dispersion relation here is still close to that of the MHD counterpart, yet we observe dissipation due to the compressive nature of the kinetic Alfvén wave.

Using the same $E(\mathbf{k})$ we find that the dissipation rate $\dot{Q}$, as defined by equation (6), is comparable (to within a factor of ~ 2) to: (i) the observed inertial range turbulent cascade rate; and (ii) the necessary *in situ* heating required for the slower-than-adiabatic radial temperature profile of the solar wind protons at 1 AU. We also find that about half the energy dissipated goes to heating electrons.

We should be a little careful of such close agreement between our results and observations, given the limitations of the assumptions that have been made in producing $E(\mathbf{k})$:

1. The ansatz in using contours of constant γ/ω might at first glance appear to be a leap of faith that leads to fortuitously good comparison with observation. We can view γ/ω as a damping strength, whereby the amplitude of the wave will decrease by a factor e in $(2\pi|\gamma/\omega|)^{-1}$ cycles [*Barnes*, 1966]. Thus we justify our ansatz by claiming that waves that damp slower than this can easily be replenished by a spectral cascade, whereas those waves that damp faster than they can be resupplied cannot remain in the inertial range. We note in passing that putting

$|\gamma/\omega| = 3 \times 10^{-3}$ and $\omega/\Omega_p = 0.14$ into the above expression yields an e-folding time of a little over 1 hour.

2. The assumption of an isotropic distribution of power in the synthetic spectrum (A_0 not a function of θ) is almost certainly incorrect, although we cannot say to what extent. Observations [*Bieber et al.*, 1996; Paper 1] suggest that 80–90% of the inertial range energy is contained in fluctuations with 2-D or quasi-2-D symmetry. Admittedly, the method used in Bieber *et al.* and Paper 1 assumed a two-component model, and did not allow for energy carried by obliquely propagating fluctuations. Even so, we find in section 5 that the wave vectors that have the most effect in determining the spectral break frequency are at highly oblique (60°–80°) angles.

3. We also do not consider the related possibilities of anisotropic spectral cascade; *i.e.*, ε is a function of θ and transfer of energy in the perpendicular direction of $\mathbf{k}$ space but not in the parallel direction [*Shebalin et al.*, 1983], or wave refraction away from parallel propagation by interaction with pressure-balanced structures of velocity shears [*Ghosh et al.*, 1998]. We do this to avoid biasing our results with detailed assumptions of the spectral anisotropy that may not be consistently supported by all events. Some degree of anisotropy seems unavoidable, but more observational work is needed for it to be more thoroughly characterized. A higher degree of spectral anisotropy may not significantly alter the computed heating rates given here as the total energy of any candidate $E(\mathbf{k})$ must be the same.

We acknowledge that at first glance, kinetic Alfvén waves would seem to be an inappropriate means of dissipating waves with $\theta_{kB} \simeq 90°$. Our assumption, which we have attempted to justify, that dissipation is controlled by γ/ω provides a fortuitous patch to this difficulty. The class of observations that seems most poorly described by this theory are the magnetic cloud events which as we have demonstrated [*Leamon et al.*, 1998b] are low-β and highly two-dimensional; therefore they are the most poorly addressed by this mechanism.

Acknowledgments

This work is supported by the Wind mission through NASA subcontract NAG5-2848 to the Bartol Research Institute. The participation of H.K.W. is supported by NASA contract NAS5-32484 and by a grant to the Goddard Space Flight Center from the NASA Space Physics Theory Program. The authors wish to thank the P.I. of the Wind Magnetic Field Investigation, R.P. Lepping, for making the data available for this study. Wind electron plasma data used in the final section was provided by R.J. Fitzenreiter, to whom we are grateful. Helpful conversations with W.H. Matthaeus are also gratefully acknowledged.

REFERENCES

1. Barnes, A., Collisionless damping of hydromagnetic waves, *Phys. Fluids*, **9**, 1483–1495, 1966.
2. Batchelor, G. K., *The Theory of Homogeneous Turbulence*, Cambridge University Press, New York, 1953.
3. Behannon, K. W., *Observations of the interplanetary magnetic field between 0.46 and 1 AU by the Mariner 10 spacecraft*, Ph.D. thesis, Catholic Univ. of Am., Washington, DC, 1975.
4. Belcher, J. W., and L. Davis, Jr., Large-amplitude Alfvén waves in the interplanetary medium, 2, *J. Geophys. Res.*, **76**, 3533–3563, 1971.
5. Bieber, J. W., W. Wanner, and W. H. Matthaeus, Dominant two-dimensional solar wind turbulence with implications for cosmic ray transport, *J. Geophys. Res.*, **101**, 2511–2522, 1996.
6. Chen, J., *Cosmic ray unidirectional latitude gradient: Evidence for north-south asymmetric solar modulation*, Ph.D. thesis, University of Delaware, Newark, 1989.
7. Coleman, P. J., Jr., Turbulence, viscosity, and dissipation in the solar wind plasma, *Astrophys. J.*, **153**, 371–388, 1968.
8. Denskat, K. U., H. J. Beinroth, and F. M. Neubauer, Interplanetary magnetic field power spectra with frequencies from 2.4×10^{-5} Hz to 470 Hz from Helios-observations during solar minimum conditions, *J. Geophys.*, **54**, 60–67, 1983.
9. Dobrowolny, M., A. Mangeney, and P. Veltri, Fully developed anisotropic hydromagnetic turbulence in interplanetary space, *Phys. Rev. Lett.*, **45**, 144–147, 1980.
10. Freeman, J. W., Estimates of solar wind heating inside 0.3 AU, *Geophys. Res. Lett.*, **15**, 88–91, 1988.
11. Gary, S. P., *Theory of Space Plasma Microinstabilities*, Cambridge Univ. Press, New York, 1993.
12. Gazis, P. R., and A. J. Lazarus, Voyager observations of solar wind proton temperature: 1–10 AU, *Geophys. Res. Lett.*, **9**, 431–434, 1982.
13. Ghosh, S., W. H. Matthaeus, D. A. Roberts, and M. L. Goldstein, The evolution of slab fluctuations in the presence of pressure-balanced magnetic structures and velocity shears, *J. Geophys. Res.*, **103**, 23 691–23 704, 1998.

14. Goldstein, M. L., D. A. Roberts, and C. A. Fitch, Properties of the fluctuating magnetic helicity in the inertial and dissipation ranges of solar wind turbulence, *J. Geophys. Res.*, **99**, 11 519–11 538, 1994.

15. Grappin, R., U. Frisch, J. Leorat, and A. Pouquet, Alfvénic fluctuations as asymptotic states of MHD turbulence, *Astron. Astrophys.*, **102**, 6, 1982.

16. Grappin, R., A. Pouquet, and J. Leorat, Dependence of MHD turbulence spectra on the velocity field-magnetic field correlation, *Astron. Astrophys.*, **126**, 51, 1983.

17. Hasegawa, A., Particle acceleration by MHD surface wave and formation of aurora, *J. Geophys. Res.*, **81**, 5083, 1976.

18. Hasegawa, A., and T. Sato, *Space Plasma Physics 1. Stationary Processes*, Springer-Verlag, New York, 1989.

19. Hasegawa, A., and C. Uberoi, The Alfvén wave, *Rep. DOE/ TIC No. 11197*, Tech. Inf. Cent., U.S. Dep. of Energy, Washington, DC, 1982.

20. Hollweg, J. V., The kinetic Alfvén wave revisited, *J. Geophys. Res.*, **104**, in press, 1999.

21. Kolmogoroff, A. N., The local structure of turbulence in incompressible viscous fluid for very large Reynolds numbers, *C. R. Acad. Sci. URSS*, **30**, 301–305, 1941.

22. Kraichnan, R. H., Inertial range of hydromagnetic turbulence, *Phys. Fluids*, **8**, 1385–1387, 1965.

23. Leamon, R. J., C. W. Smith, N. F. Ness, W. H. Matthaeus, and H. K. Wong, Observational constraints on the dynamics of the interplanetary magnetic field dissipation range, *J. Geophys. Res.*, **103**, 4775–4787, 1998a.

24. Leamon, R. J., C. W. Smith, and N. F. Ness, Characteristics of Magnetic Fluctuations Within Coronal Mass Ejections: The January 1997 Event, *Geophys. Res. Lett.*, **25**, 2505–2508, 1998b.

25. Leamon, R. J., W. H. Matthaeus, C. W. Smith, and H. K. Wong, Contribution of cyclotron-resonant damping to kinetic dissipation of interplanetary turbulence, *Astrophys. J. Lett.*, **507**, L181–L184, 1998c.

26. Lepping, R. P., *et al.*, The WIND magnetic field investigation, *Space Sci. Rev.*, **71**, 207–229, 1995.

27. Lysak, R. L., and W. Lotko, On the kinetic dispersion relation for shear Alfvén waves, *J. Geophys. Res.*, **101**, 5085–5094, 1996.

28. Marsch, E., Kinetic physics of the solar wind plasma, in *Physics of the Inner Heliosphere 2. Particles, Waves and Turbulence*, pp. 45–133, edited by R. Schwenn and E. Marsch, Springer-Verlag, New York, 1991.

29. Matthaeus, W. H., and Y. Zhou, Extended inertial range phenomenology of magnetohydrodynamic turbulence, *Phys. Fluids B*, **1**, 1929–1933, 1989.

30. Matthaeus, W. H., S. Ghosh, S. Oughton, and D. A. Roberts, Anisotropic Three-Dimensional MHD Turbulence *J. Geophys. Res.*, **101**, 7619, 1996.

31. Matthaeus, W. H., C. W. Smith, and S. Oughton, Dynamical age of solar wind turbulence in the outer heliosphere, *J. Geophys. Res.*, **103**, 6495–6502, 1998.

32. Matthaeus, W. H., G. P. Zank, C. W. Smith, and S. Oughton, Turbulence, spatial transport, and heating of the solar wind, *Phys. Rev. Lett.*, **82 (17)**, in press, 1999.

33. Ogilvie, K. W., *et al.*, SWE, A comprehensive plasma instrument for the WIND spacecraft, *Space Science Reviews*, **71**, 55–77, 1995.

34. Richardson, J. D., K. I. Paularena, A. J. Lazarus, and J. W. Belcher, Radial evolution of the solar wind from IMP 8 to Voyager 2, *Geophys. Res. Lett.*, **22**, 325–328, 1995.

35. Roberts, D. A., M. L. Goldstein, L. W. Klein and W. H. Matthaeus, Origin and evolution of fluctuations in the solar wind: Helios observations and Helios-Voyager comparisons, *J. Geophys. Res.*, **92**, 12 023–12 035, 1987.

36. Schwartz, S. J., W. C. Feldman, and S. P. Gary, The source of proton anisotropy in the high-speed solar wind, *J. Geophys. Res.*, **86**, 541–546, 1981.

37. Shebalin, J. V., W. H. Matthaeus, and D. C. Montgomery, Anisotropy in MHD turbulence due to a mean magnetic field, *J. Plasma Phys.*, **29**, 525–547, 1983.

38. Smith, C. W., W. H. Matthaeus, and N. F. Ness, Measurement of the dissipation range spectrum of magnetic fluctuations in the solar wind with applications to the diffusion of cosmic rays, *Proc. Int. Conf. Cosmic Ray 21st*, (5), 280–283, 1990.

39. Tu, C.-Y., The damping of interplanetary Alfvénic fluctuations and the heating of the solar wind, *J. Geophys. Res.*, **93**, 7–20, 1988.

40. Williams, L. L., G. P. Zank, and W. H. Matthaeus, Dissipation of pickup-induced waves: A solar wind temperature increase in the outer heliosphere?, *J. Geophys. Res.*, **100**, 17 0599–17 067, 1995.

41. Zank, G. P., W. H. Matthaeus, and C. W. Smith, Evolution of turbulent magnetic fluctuation power with heliospheric distance, *J. Geophys. Res.*, **101**, 17 093–17 107, 1996.